J Nanopart Res (2021) 23: 40
https://doi.org/10.1007/s11051-021-05154-z

RESEARCH PAPER

Hydrothermal synthesis of N, P co-doped graphene quantum dots for high-performance Fe^{3+} detection and bioimaging

Yongsheng Yang · Bingli Gu · Zhiduo Liu · Da Chen · Yun Zhao · Qinglei Guo · Gang Wang

Received: 15 September 2020 / Accepted: 25 January 2021 / Published online: 3 February 2021

Abstract Doped carbon-based materials have attracted considerable attentions due to their extraordinary optical, thermal, and electronic properties. Herein, we demonstrate a facile and universal approach, which involves the hydrothermal treatment of citric acid and phosphonitrilic chloride trimer ($Cl_6N_3P_3$), for the production of nitrogen and phosphorus co-doped graphene quantum dots (N, P-GQDs). The obtained N, P-GQDs with a mean size of about 3.4 nm exhibit bright yellow fluorescence, good-solubility, and attractive optical stability. Although the quantum yield as high as 34.8% has been proved in our synthesized N, P-GQDs, the fluorescence can be also fleetly and selectively quenched by Fe^{3+} ions. Therefore, high-performance Fe^{3+} sensors are fabricated with N, P-GQDs, with an ultra-sensitive detection limit of 146 nM. Furthermore, high ionic strength, mild acids, and alkaline are demonstrated to have a small impact on the fluorescence intensity of the N, P-GQDs. Finally, the as-synthesized N, P-GQDs, with bright luminescence and excellent biocompatibility, are applied for bioimaging, e.g., fibroblast cells.

Keywords Graphene quantum dots · Photoluminescence · High quantum yield · Bioimaging

Y. Yang · B. Gu · D. Chen (✉) · G. Wang (✉)
Department of Microelectronic Science and Engineering, School of Physical Science and Technology, Ningbo University, Ningbo 315211, People's Republic of China
e-mail: chenda@nbu.edu.cne-mail: gangwang@nbu.edu.cn

Z. Liu
State Key Laboratory of Integrated Optoelectronics, Institute of Semiconductors, Chinese Academy of Sciences, Beijing 100083, People's Republic of China

Y. Zhao
Faculty of Electrical Engineering and Computer Science, Ningbo University, Ningbo 315211, People's Republic of China

Q. Guo (✉)
School of Microelectronics, Shandong University, Jinan 250100, People's Republic of China
e-mail: qlguo@sdu.edu.cn

Introduction

Graphene quantum dots (GQDs), as one of the newly developed members of carbon material family, have attracted wide attentions, since it is first discovered in the purification of single-wall carbon nanotubes (Novoselov et al. 2004). Owing to the pronounced quantum confinement and edge effects, GQDs present extraordinary optical, thermal, and electronic properties which are not obtainable in other kinds of semiconductor quantum dots and organic dyes (Zhang et al. 2016; Li et al. 2015a; Xu et al. 2018a). These unique physicochemical properties make them potential candidates for applications in several fields such as fluorescent sensing (Yuan et al. 2015; Chen et al. 2017; Wang et al. 2016), fluorescent bioimaging (Wang et al. 2020a; Hai et al. 2018), photocatalysis (Zeng et al. 2018; Khojasteh et al. 2020), and photovoltaic conversion (Chang et al. 2019; Zhao et al. 2014; Haider et al. 2016). Currently, to enhance the fluorescence of GQDs, particularly in

increasing the emission efficiency, numerous approaches have been proposed to synthesize modified GQDs with monobasic or dualistic dopants. As being recently demonstrated, heteroatom doping (oxygen, boron, nitrogen, phosphor, sulfur, etc.) can change various properties of GQDs including electronic structure, band gap, chemical reactivity, and optical properties (Ma et al. 2020; Sim et al. 2020). Without surface passivation and/or doping, the quantum yield of GQDs is quite low (Zhang et al. 2019). Among these heteroatom-doped GQDs, nitrogen is considered as a promising candidate for the dopant because of their comparable atomic size to carbon and five available valence electrons for bonding with carbon atoms. (Xu et al. 2018b) More recently, plenty of works have been done toward designing co-doping multiple heteroatoms for further improving the optical and electrical properties of GQDs due to the synergistic effect of doped heteroatoms in GQDs (Kaur et al. 2018). For example, D. Qu et al. demonstrated the success of synthesizing S, N co-doped GQDs, which is further utilized for visible light photocatalysts (Qu et al. 2013). B, N, S co-doped GQDs were obtained by Liu et al. with 2, 5-diaminobenzene sulfonic acid and 4-aminophenylboronic acid hydrochloride, exhibiting a strong long-wavelength emission band (Liu et al. 2017a). Rongjun et al. prepared N, P-GQDs by utilizing tetrakis (hydroxymethyl) phosphonium chloride and ethylenediamine endcapped polyethylenimine, which are functionalized as probes toward nitrite detection in live cell. (Liu et al. 2017b) Though only few studies covered N, P-GQDs, the N, P co-doping in GQDs might greatly extend the arsenal of GQDs and their potential applications. New and unanticipated properties of GQDs can be produced by doping them with nitrogen and phosphorus atoms, with more active sites and modified electronic characteristics (Shi et al. 2016). Therefore, a simple and convenient approach for the production of N, P-GQDs with high crystal quality is highly desired, and systematic investigations on the properties and potential applications are also necessary.

It is known that optimal uptake of trace elements performs crucial roles in cellular metabolism, enzyme catalysis, oxygen transport of hemoglobin, and enzyme-based reactions as a cofactor (Liu et al. 2017a; Shi et al. 2016). Iron ions (Fe^{3+}) are important to numerous biological processes. Fe^{3+} provides the oxygen-carrying capacity of heme and acts as a cofactor in many enzymatic reactions (Atchudan et al. 2018a). However, Fe^{3+} overload and deficiency can disturb the cellular homeostasis, thus resulting in various diseases, such as anemia, arthritis, intelligence decline, heart failure, diabetes, and cancer (Gao et al. 2018). Therefore, it is highly desired to develop sensitive and selective sensing strategies for Fe^{3+} monitoring in aqueous solutions, as well as in living cells.

On the basis of the above reasons, we proposed a fluorescent nanosensor based on N, P-GQDs, which are synthesized by using citric acid and phosphonitrilic chloride trimer ($Cl_6N_3P_3$), for the sensitive and selective monitoring of Fe^{3+} in aqueous solution and living cells (Fig. 1). The as-prepared N, P-GQDs possess strong fluorescence with the PL quantum yield as high as 34.8%. Moreover, the N, P-GQDs exhibit yellow emission, uniform size, and excitation-dependent photoluminescence behavior. Owing to the modified electronic characteristics by doping with nitrogen and phosphorus atoms, a label-free chemosensor based on the as-prepared N, P-GQDs has been developed, with a sensitive response to Fe^{3+} in the concentration range of

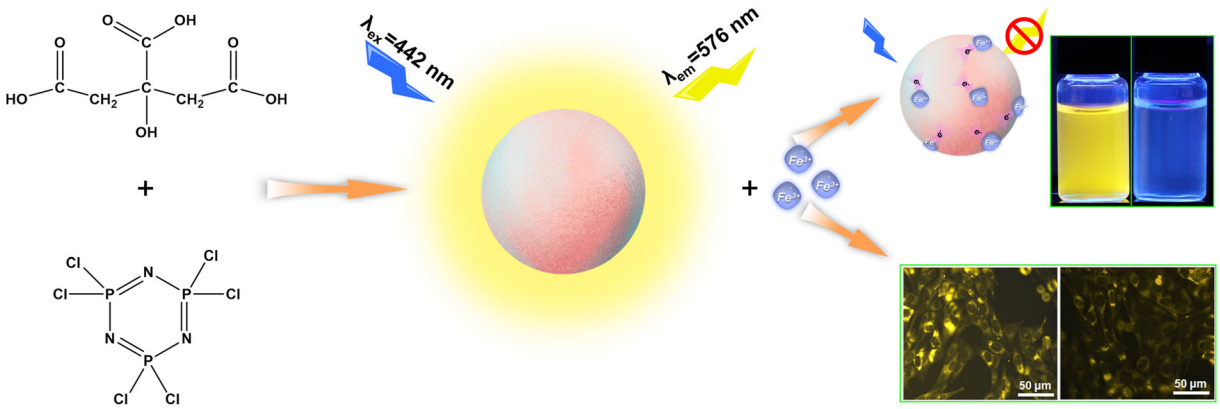

Fig. 1 Synthesis of N, P-GQDs and its sensing performance for the detection of Fe^{3+} in aqueous solution and living cells

0–150 nM and a detection limit of 146 nM. Significantly, the as-prepared N, P-GQDs possess negligible cytotoxicity and excellent biocompatibility in fibroblast cells. The results reported here provide a better understanding of the quenching mechanism for Fe^{3+} ions and expand the application of as-prepared N, P-GQDs in sensing and environmental fields.

Materials and methods

Materials

All chemicals used in this work were of analytical grade. Citric acid, phosphonitrilic chloride trimer, $FeCl_3$, $FeCl_2$, $CuCl_2$, $CaCl_2$, $CoCl_2$, $Zn(NO_3)_2$, $AgNO_3$, $Ni(NO_3)_2$, $CdCl_2$, Li_2SO_4, $MgSO_4$, KCl, NaCl, $PdCl_2$, $Al(NO_3)_3$, $MnCl_2$, and $HgCl_2$ were purchased from Aladdin Chemistry Co. Ltd. (Shanghai, China). All chemical solvents and reagents are used as-received without any additional purification. Water used throughout all experiments was purified by the Millipore system.

Characterization methods

Transmission electron microscopy (TEM) was carried out on Hitachi H-8100 at 200 kV accelerating voltage. X-ray photoelectron spectroscopy (XPS) was measured on PHI Quantera II system, Fourier transform infrared (FTIR) spectra was measured using a Thermo Scientific Nicolet 6700 FTIR spectrometer. Atomic Force Microscope (Cypher S, Asylum research) was used to determine the height profiles of N, P-GQDs. Ultraviolet-visible (UV-Vis) absorption properties were recorded by a UV-5800 spectrophotometer. Photoluminescence (PL) and photoluminescence excitation (PLE) spectra were collected on a PerkinElmer LS55 luminescence spectrometer (PerkinElmer Instruments, U.K.) at room temperature. PL lifetime was measured via the time-correlated single-photon counting (TCSPC) technique (HydraHarp 400, Pico Quant).

Synthesis of N, P-GQDs

A hydrothermal method was used to prepare the N, P-GQDs. Firstly, 0.084 g citric acid and 0.016 g phosphonitrilic chloride trimer ($Cl_6N_3P_3$) were dissolved in 10 mL alcoholic solution thoroughly to form a clear solution. Then, the solution was transferred into a 50-mL Teon-lined stainless steel autoclave and heated at 180 °C for 48 h. After being cooled to room temperature naturally, the resulting deep-brown aqueous dispersion was centrifuged for 15 min at 12 000 rpm/min to dislodge nonfluorescent deposit, and then dialyzed for 72 h in a dialysis membrane (100~500 Da) against DI water for purification. Under vacuum condition, the prepared N, P-GQDs were then dried for 48 h at room temperature and stored at 4 °C for the following use.

Measurement of quantum yield (φ)

The quantum yield (φ) of GQDs was estimated by comparing the integrated PL intensities and the absorbency values against the reference quinine sulfate (φ = 0.54). Briefly, the absorbance for the quinine sulfate and the N, P-GQDs at the 360 nm excitation and the fluorescence spectra of the same solutions at the same excitation were measured respectively. Then, the integrated fluorescence intensity from the fluorescence spectrum was calculated. The quantum yield was calculated according to Eq. (1): (Wang et al. 2020b)

$$\varphi = \varphi_R \times \frac{I}{I_R} \times \frac{A_R}{A} \times \frac{\eta^2}{\eta_R^2} \quad (1)$$

where φ is the quantum yield, I is the measured integrated emission intensity, η is the refractive index of the solvent, A is the optical density, and the subscript R refers to the reference standard with a known quantum yield.

Detection of Fe^{3+} using N, P-GQDs

The detection of Fe^{3+} was performed at room temperature in 10 mM phosphate-buffered saline (PBS, pH = 7). In a typical assay, 200 μL of N, P-GQDs dispersion (5 mg/mL) was added into 2 mL of PBS, followed by the addition of Fe^{3+} standard with various concentrations (10 μL). The fluorescence emission spectra were recorded after reaction for 5 min at room temperature. The sensitivity and selectivity measurements were conducted in triplicate. The selectivity of Fe^{3+} sensing was confirmed by adding other common metal ions stock solutions (including H^+, Li^+, Na+, K^+, Mg^{2+}, Ca^{2+}, Fe^{2+}, Co^{2+}, Ni^{2+}, Cu^{2+}, Zn^{2+}, Cd^{2+}, Hg^{2+}, Ag^+, Pb^{2+}, Al^{3+}, Mn^{2+} ions) instead of Fe^{3+} in a similar way.

Cellular imaging

Fibroblast cells grown on 18 × 18 mm^2 glass coverslips were first cultured in Dulbecco's modified Eagle's medium (DMEM, Thermo Fisher Scientific) supplemented with 10% fetal bovine serum (FBS), 100 $mg{\cdot}mL^{-1}$ glutamine, 100 $mg{\cdot}mL^{-1}$ sodium pyruvate, penicillin (100 $units{\cdot}mL^{-1}$), and streptomycin (100 $units{\cdot}mL^{-1}$) at 37 °C in a humidified atmosphere overnight followed by incubation with 300 $\mu g{\cdot}mL^{-1}$ N, P-GQDs for 24 h. For assessing Fe^{3+} uptake, fibroblast cells were incubated with 300 $\mu g{\cdot}mL^{-1}$ N, P-GQDs for 24 h as described above, followed by incubation with 80 μM $FeCl_3$ for 6 h at 37 °C. Finally, cell imaging was performed with Zeiss LSM 780 confocal lasers scanning fluorescence microscopy.

Results and discussion

Characterization of N, P-GQDs

The size distribution and morphology of the N, P-GQDs are characterized by TEM. As shown in Fig. 2a, the prepared N, P-GQDs have a regular spherical shape and are well separated from each other. According to the size

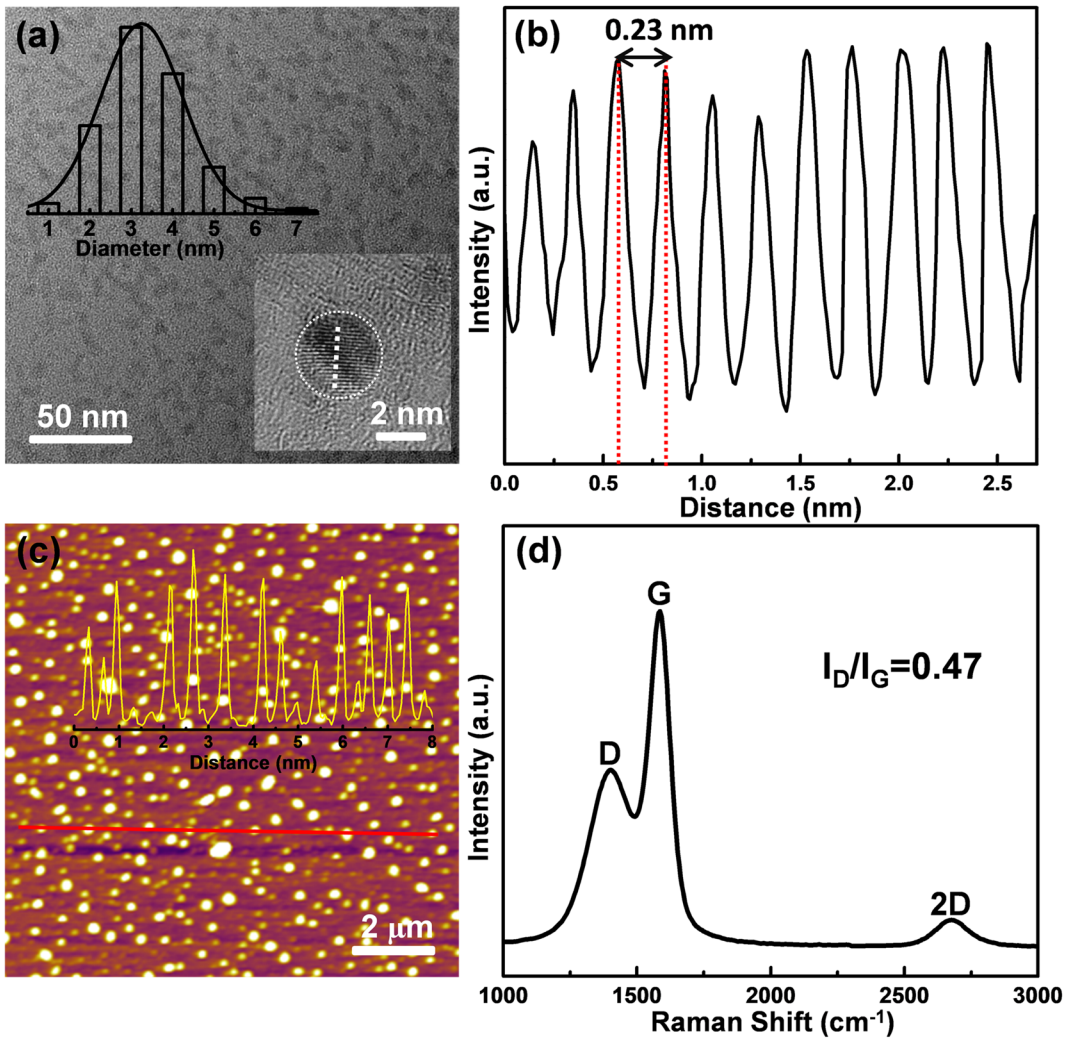

Fig. 2 **a** Plan-view TEM image of the as-prepared N, P-GQDs. The insets correspond to the size distribution histogram (top) and HRTEM image of N, P-GQDs (bottom). **b** Line-cut result of the HRTEM image of N, P-GQDs. **c** AFM image of the N, P-GQDs spin-coated on a SiO_2/Si substrate. The inset shows the thickness variations of N, P-GQDs along the horizontal direction. **d** Typical Raman spectrum of N, P-GQDs on a SiO_2/Si substrate

distribution histogram (Fig. 2a inset, obtained by counting about 200 particles), the average particle size of N, P-GQDs is estimated as 3.4 nm. High-resolution TEM (HRTEM) image (Fig. 2a inset) shows clear lattice structure of the N, P-GQDs, confirming the highly crystalline structure. A line cutting (white dotted line in Fig. 2a) is performed to extract the lattice parameter of ~0.23 nm (Fig. 2b), which is consistent with the [1120] lattice fringes of graphite (Zhu et al. 2015). Figure S1 exhibits the fast Fourier transform (FFT) analysis pattern, and an obvious orthohexagonal symmetry is seen, suggesting that the N, P-GQDs are almost defect-free graphene. Figure 2 c shows a representative AFM image of the N, P-GQDs after spin coating on a SiO_2/Si substrate. The thickness extracted in the AFM topography is around 0.5–0.84 nm with an average value of 0.71 nm, which indicates that most of the N, P-GQDs is 1~2 layers. In addition, Raman scattering spectroscopy is also used to characterize the N, P-GQDs (Fig. 2d), where three primary peaks are emerged. The defect-related D and G bands are centered at 1350 cm^{-1} and 1577 cm^{-1}, respectively, whereas the 2D peak (~2700 cm^{-1}) is strongly suppressed. The relative intensity of the D band to G band (I_D/I_G) for the GQDs is 0.47, which indicates the well crystallized sp^2 structure of as-prepared N, P-GQDs. Structural properties of N, P-GQDs are also characterized by XRD analysis. Figure S2 shows a broad peak between 15 and 50°, with a peak at around 23.8°. It can be concluded that the prepared N, P-GQDs are microcosmic crystalline carbon.

The chemical components and structures of the N, P-GQDs are investigated by the XPS analysis. C 1s, N 1s, O 1s, and P 2p signals appeared at 285.0 eV, 398.5 eV, 530.5 eV, and 132.9 eV are observed in the XPS spectrum (as shown in Fig. 3a). In addition, composition analysis of the N, P-GQDs indicates that the C, N, P, and O compositions are 73.6%, 5.1%, 6.2%, and 15.1%. The doping percentages of N and P are much higher than that of previously reported N, P-GQDs (Sun et al. 2015). The high-resolution C 1s XPS spectrum (Fig. 3b) is well-fitted into C-C/C=C bonds (284.2 eV), C-N/C-P bonds (285.7 eV), and -COOH bond (287.4 eV). The peak of the high-resolution spectrum of N 1s (Fig. 3c) is fitted into three peaks at 397.3 eV, 398.8 eV, and 400.3 eV, which are assigned to C-N, C=N, and N-P bonds, respectively. The P 2p XPS spectrum (Fig. 3d) can be divided into two peaks at 133.7 and 134.8 eV, corresponding to C=P and C-P/N-P, respectively. These results illustrate that nitrogen and phosphorus atoms are covalently bonded in the N, P-GQDs during the synthesis process. As shown in Fig. 3e, the high-resolution spectrum of O 1s in the N, P-GQDs can be fitted with three species of -COOH (531.2 eV), C=O (532.3 eV), and C-OH/C-O-C (533.6 eV), indicating the surfaces of N, P-

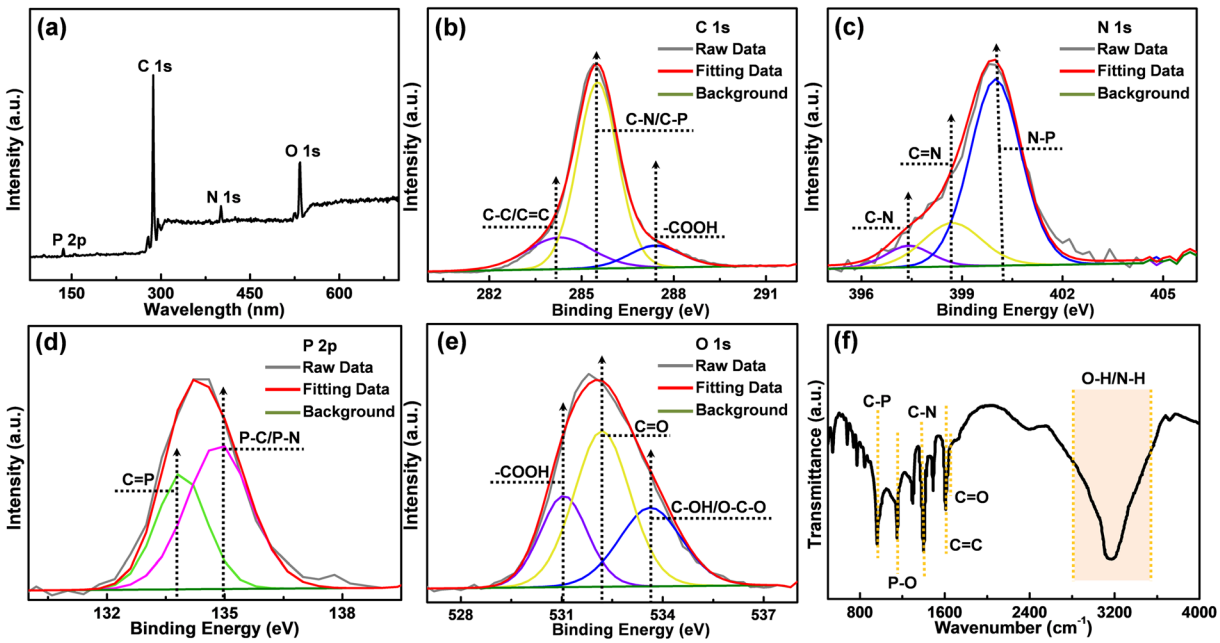

Fig. 3 Chemical structure analysis of N, P-GQDs: **a** fully scanning XPS spectrum of N, P-GQDs, high-resolution XPS spectrum of **b** C 1s, **c** N 1s, **d** P 2p, and **e** O 1s spectrum. **f** FTIR spectrum of N, P-GQDs

GQDs are filled with hydrophilic groups (hydroxyl and carboxylic groups), which ensures the good water solubility of the prepared N, P-GQDs. The FTIR analysis is performed to investigate surface functional groups of obtained N, P-GQDs. In the Fig. 3f, the absorption bands at 3190 cm^{-1} and 3250 cm^{-1} are ascribed to the stretching vibration of O-H and N-H, respectively. The band at 1685 cm^{-1} is attributed to the stretching vibrations of C=O. The peak at 1608 cm^{-1} indicates the existence of C=C stretching vibration (Jia et al. 2019). Typically, the sharp peaks at 1048 cm^{-1}, 1190 cm^{-1}, and 1400 cm^{-1} are attributed to C-P, P-O, and C-N, respectively, which is consistent with the results from XPS. All results of XPS and FTIR spectra clearly confirm the success of co-doping N and P atoms in GQDs.

Optical properties of N, P-GQDs

The optical properties of the N, P-GQDs are investigated. Figure 4 a shows the UV-vis absorption spectrum and fluorescent spectrum of N, P-GQDs aqueous solution. Typical π-π* transition (sp^2 domains in N, P-GQDs) and n-π* transition (between N, P-doped atoms and sp^2 carbon atoms) absorption bands are found around at ~223 and ~306 nm, respectively (Luo et al. 2016; Chen et al. 2018). The UV-vis absorption spectrum shows a long tail extending into the visible range. This indicates the considerable absorption in visible light range. Additionally, the maximum emission spectrum with a peak position at 576 nm (blue curve) obtained with an excitation wavelength of 442 nm (red

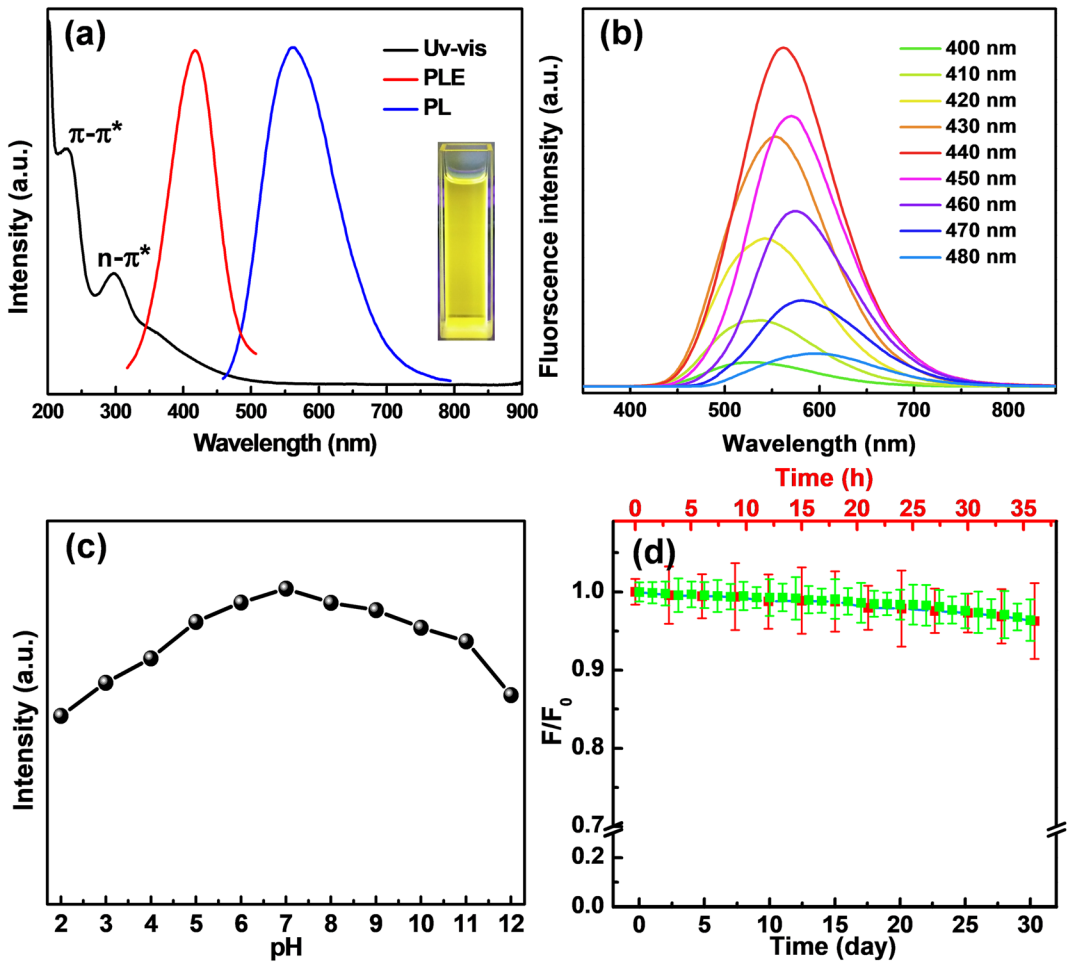

Fig. 4 Optical properties of N, P-GQDs. **a** UV-vis absorption (black line), fluorescence excitation (red line) and emission (blue line) spectra of N, P-GQDs. The inset corresponds to the optical image of N, P-GQDs aqueous solution under 365 nm UV light irradiation. **b** Emission spectra of N, P-GQDs at different excitation wavelength from 370 to 530 nm. The effects of **c** pH, **d** continuous UV irradiation, and visible light irradiation on the fluorescence intensity of N, P-GQDs

curve) suggests a yellow emission behavior for the synthesized N, P-GQDs. It is further evidenced by the distinct yellow light emission from the N, P-GQDs aqueous solution when irradiated under UV light (as shown in Fig. 4a inset). Figure 4 b presents the PL spectra of N, P-GQDs at different excitation wavelengths in aqueous solution, indicating that a maximum emission wavelength of 572 nm can be obtained with the excitation wavelength of 440 nm. Furthermore, the emission spectra of N, P-GQDs are gradually red-shifted to higher wavelengths accompanied by first an increase and then a decrease of fluorescence intensities. The excitation-dependent fluorescence behavior of N, P-GQDs may be resulted from the variations in size and surface state (Yan et al. 2019). In Fig. 4c, the effect of pH on the N, P-GQDs was also investigated. It is obvious that the PL intensity of N, P-GQDs (at λ_{max} = 576 nm) increases from pH 2 to 7, then decreases as the further increase of the pH value (up to pH = 12), indicating that the neutral condition that pH = 7 is more favorable for fluorescence detection. Meanwhile, with continuous UV irradiation (150 W mercury lamp with a center wavelength of 320 nm) and visible light irradiation, no obvious photo-bleaching is observed (Fig. 4d), demonstrating the excellent photostability of N, P-GQDs. In addition, the effect of ionic strength on the fluorescence intensity of N, P-GQDs is explored in the Figure S3, which shows that varying the NaCl concentration from 0.1 to 1 M has little effect on the fluorescence signal of N, P-GQDs. Moreover, the quantum yield (φ) of the N, P-GQDs in this work reaches up to 34.8% with standard quinine sulfate as the reference, which is comparable to the previously reported N, P-GQDs (Shi et al. 2016; Li et al. 2015b).

Detection of Fe^{3+} using N, P-GQDs

In order to enhance the performance for Fe^{3+} assay, the effects of pH and reaction time are optimized. As shown in Figure S4, the optimal pH value and reaction time are found to be 7 and 90 s, respectively. Moreover, the selectivity and competition experiments are also performed. As illustrated in Fig. 5a, the quenching of fluorescence intensity of N, P-GQDs in the presence of 80 μM metal ions, including H^+, Li^+, Na+, K^+, Mg^{2+}, Ca^{2+}, Fe^{2+}, Fe^{3+}, Co^{2+}, Ni^{2+}, Cu^{2+}, Zn^{2+}, Cd^{2+}, Hg^{2+}, Ag^+, Pb^{2+}, Al^{3+}, Mn^{2+}, and some anions, is analyzed after incubation of 5 min. From the results, except for Fe^{3+}, only Cu^{2+} has small quenching effect on fluorescence intensity, which can be attributed to the adsorption of metal ion into GQDs (Dutta Chowdhury and Doong 2016). As shown in Figure 5b, the color of the N, P-GQDs solution changes from yellow to faint blue after adding different concentrations of Fe^{3+} and can be vividly seen by the unaided eye under UV light. Meanwhile, Fig. 5 c shows the change in fluorescence intensity of N, P-GQDs solutions after the addition of various concentrations of Fe^{3+} ranging from 0 to 300 μM. The quenching of fluorescence intensity of N, P-GQDs increases with the increase of the Fe^{3+} concentration. The calibration plot of the change in fluorescence intensity $(F_0–F)/F_0$ as a function of Fe^{3+} concentration is shown in Fig. 5d, where the F_0 and F were the PL intensities of N, P-GQDs at $\lambda_{ex}/\lambda_{em}$ of 442/576 nm in the absence and presence of Fe^{3+}, respectively. The change in fluorescence intensity increases rapidly in the low concentration range of Fe^{3+} and then increases slowly to a plateau when Fe^{3+} concentration increases up to 100 μM. The inset of Fig. 5d shows a good linear relationship between the $(F_0–F)/F_0$ and Fe^{3+} concentration ranging from 0 to 150 nM. The limit of detection (LOD), determined by the 3δ/S (δ is the standard deviation of the lowest signal and S is the slope of linear calibration plot), is 146 nM, which is comparable with or higher than other nanomaterial-based fluorescent sensors for Fe^{3+} detection as shown in Table 1 (Yang et al. 2020; Kagit et al. 2014; Gong et al. 2020; Liu et al. 2020; Wang et al. 2012; Pu et al. 2020; Atchudan et al. 2018b; Lu et al. 2015). To verify whether N-P doping plays a vital role, the control experiment that involves the investigation of un-doped GQDs was performed. In particular, the $Cl_6N_3P_3$ is removed from the raw materials and other conditions are unchanged. Figure S5 shows the fluorescence (at 463 nm) of un-doped GQDs solutions varying with Fe^{3+} with different concentrates in the range of 0–300 μM. It is clear that addition of Fe^{3+} has no obvious influence on the fluorescence intensity (at 463 nm) as well as the peak emission position of un-doped GQDs solutions.

The quenching mechanism of Fe^{3+} to the fluorescence of N, P-GQDs reveals the reasons for its high sensitivity and selectivity. As shown in Fig. 6a, the fluorescence quenching is fitted by a typical Stern-Volmer equation, i.e., $F_0/F = 1 + K_{SV}[Fe^{3+}]$, where K_{SV} is the Stern-Volmer quenching constant. According to the equation above, the K_{SV} is estimated to be 5.83×10^6 M^{-1}, indicating the excellent quenching effect of Fe^{3+} on the fluorescence of N, P-GQDs. In

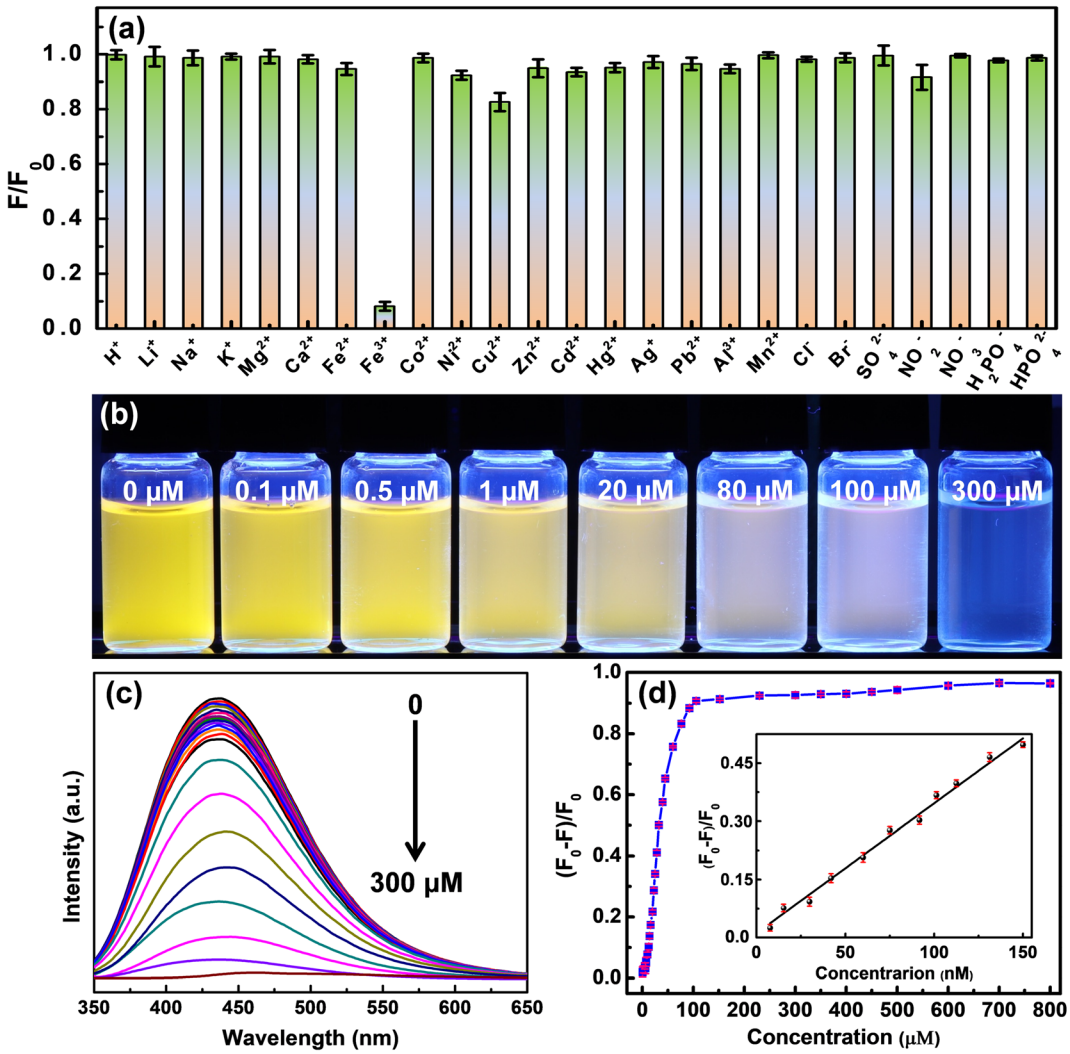

Fig. 5 Fe^{3+} detection of N, P-GQDs. **a** The selectivity of N, P-GQDs to various metal ions (80 μmol/L); *F* and F_0 is the PL intensity of N, P-GQDs with and without the present of the metal ion. **b** Optical images of N, P-GQDs solution in the presence of various concentrations of Fe^{3+} under 365 nm UV light. **c** Fluorescence spectra of N, P-GQDs at various concentrations of Fe^{3+} ranging from 0 to 300 μM. The excitation wavelength is fixed at 442 nm. **d** The change in fluorescence intensity as a function of Fe^{3+} concentration. Inset: linear relationship between fluorescence and low level Fe^{3+} concentration at 0–150 nM

view of the fact that both dynamic quenching effect and static quenching effect fit well with Stern-Volmer equation; thus, they could not be simply differentiated by using this equation. To better understand the Fe^{3+}-induced fluorescence quenching mechanism, we investigate the PL decay of N, P-GQDs which is fitted by a bi-exponential function (as shown in Fig. 6b). The average PL lifetime of N, P-GQDs is calculated to be 3.36 ns, and the lifetime became shorter with the addition of 10 μM Fe^{3+} (3.15 ns) and 30 μM Fe^{3+} (2.95 ns). Because the fluorescence lifetime of the fluorescent materials would not change during the static quenching process; therefore, the present fluorescence quenching is primarily attributed to dynamic quenching effect, which agrees with previous reports (Wang et al. 2020b). Furthermore, the zeta potentials of N-GQDs with various concentrations of Fe^{3+} are conducted to confirm the interaction between them. As shown in Fig. 6c, the zeta potentials of N, P-GQDs decrease gradually from −38.8 to −11.4 mV as the Fe^{3+} concentration increases. These results demonstrate the occurrence of electron transfer between the electron-rich group of the N, P-GQDs and the electron-deficient Fe^{3+} ions. Figure 6 d shows a

Table 1 Comparison of different fluorescent probes for Fe^{3+} detection

Type of probe	Fluorescent probes	Detection limit (μM)	Reference
Organic-based probe	Eu-polymer	0.21	(Yang et al. 2020)
	Phosphazene	4.8	(Kagit et al. 2014)
	Benzothiazole	5.86	(Gong et al. 2020)
	N, N-dithenoyl-rhodamine	3.76	(Liu et al. 2020)
GQD-based probe	Allylamine GO	4.6	(Wang et al. 2012)
	Phe-GQDs	0.72	(Pu et al. 2020)
	N-GQDs	1.2	(Atchudan et al. 2018b)
	N, S-GQDs	0.8	(Lu et al. 2015)
	N, P-GQDs	0.146	This work

representative electronic transmission. When the distance between the N, P-GQDs and Fe^{3+} ions is close enough, electrons in the excited state of N, P-GQDs would transfer to the unfilled orbit of Fe^{3+}, leading to nonradiative electron/hole recombination, and the fluorescence quenching of N, P-GQDs (Fu et al. 2019).

Intracellular imaging of Fe^{3+}

Besides the selectivity and sensitivity mentioned above, ion competition is another important parameter to evaluate the performance of the sensing system in terms of practical applications. Therefore, the competition and

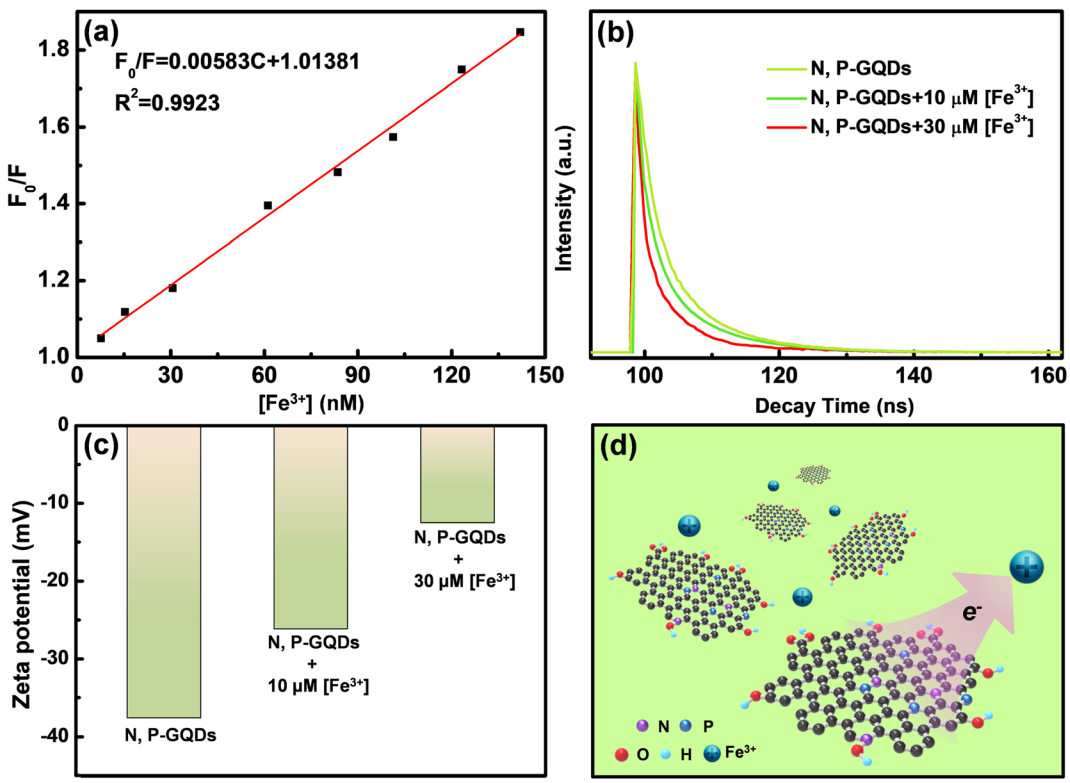

Fig. 6 Investigations on the Fe^{3+} sensing mechanism. **a** Relationship between F_0/F and the concentration of Fe^{3+}, which is fitted by a typical Stern-Volmer equation. **b** Fluorescence decay traces of N-GQDs with various concentrations of Fe^{3+}. **c** Zeta potentials of N-GQDs toward different Fe^{3+} concentrations (10 and 30 μM). **d** Schematic of the mechanism for the electronic transmission between the N, P-GQDs and Fe^{3+} ions

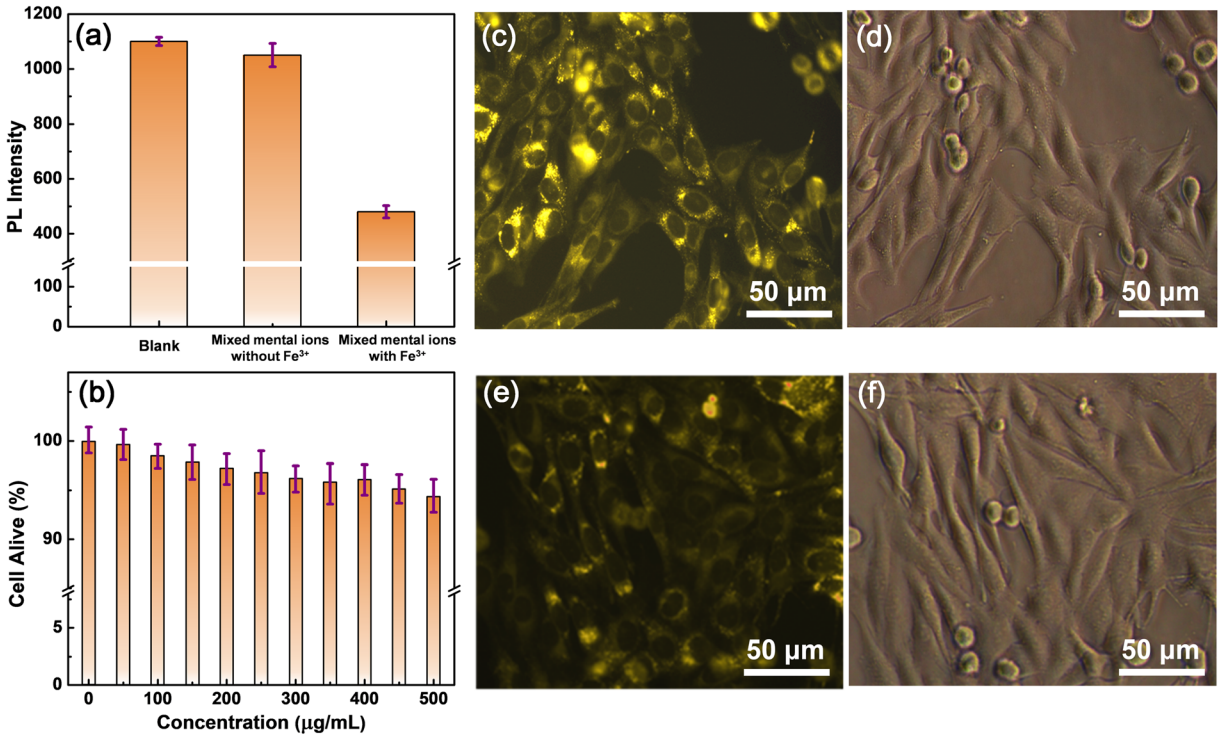

Fig. 7 Detection of Fe^{3+} in biological sample. **a** The difference in PL intensity of N, P-GQDs dispersion under various competitive metal ions (the concentration of each metal ion in the mixture was 4×10^4 nM). **b** The viability of fibroblast cells in different N, P-GQDs concentrations. Fluorescence microscopy images of fibroblast cells after incubation with: **c** N, P-GQDs, **d** N, P-GQDs+80 μM Fe^{3+} in pH = 7.4 PBS buffer. Right: the corresponding bright-field transmission images of fibroblast cells

efficiency of N, P-GQDs in the presence of all possible interference ions are evaluated considering the cross reactivity. As demonstrated in Fig. 7a, it is clear that the addition of various metal ions does not influence the quenching effect of Fe^{3+} on the fluorescence intensity, indicating that the N, P-GQD-based sensing probes possess high selectivity against other competitive metal ions (the concentration of each metal ion in the mixture is 2×10^4 nM). In addition, Fig. 7 b shows that the cell viabilities are more than 94% even with the addition of N, P-GQDs with a high dose of 500 μg/mL for 24 h, indicating the low toxicity and superior biocompatibility of the N, P-GQDs, which confirms of the possibilities N, P-GQDs in detecting Fe^{3+} in living cells. Finally, the fluorescence quenching of N, P-GQDs is applied to the Fe^{3+} analysis in fibroblast cells through MTT assays. As displayed in Fig. 7c, d, the intracellular region exhibits a noticeable yellow emission, while N, P-GQDs-stained cells also maintain good morphologies. This result reveals that the fluorescence signals are emitted from the perinuclear regions of the cytosol, indicating excellent cell-permeability of the N, P-GQDs. When the concentration of Fe^{3+} is 80 μM (Fig. 7e, f), the yellow fluorescence becomes weaker, indicating that the proposed sensor could be applied for effectively semiquantitative imaging Fe^{3+} in live cells.

Conclusions

In this study, we have successfully synthesized N, P-GQDs by using one-step citric acid and phosphonitrilic chloride trimer coupling reaction, which are further demonstrated for the applications in Fe^{3+} detection and bioimaging. Remarkably, the obtained N, P-GQDs have high quantum yield (about 34.8%), strong yellow photoluminescent, low cytotoxicity, good biocompatibility, and photostability. Besides, a simple, reliable, and sensitive Fe^{3+} ion detection is rendered by the N, P-GQDs sensing system, with the detection limit reaching to 146 nM. And a good linear correlation ($R^2 = 0.992$) over the concentration range of 0–150 nM is revealed, demonstrating the reliability and stability of the N, P-GQD-based sensing system for detecting Fe^{3+}. Finally, bioimaging and semiquantitative access of Fe^{3+} concentration in live cells are demonstrated by our synthesized

N, P-GQDs. This study provides guideline for better understanding of the quenching mechanism of N, P-GQDs, and for the design of high-performance GQD-based sensors.

Supplementary Information The online version contains supplementary material available at https://doi.org/10.1007/s11051-021-05154-z.

Funding This work was supported by projects from the National Natural Science Foundation of China under grant nos. 11704204, 61604084, and 51802337; K. C. Wong Magna Fund in Ningbo University; and the Natural Science Foundation of Ningbo under grant no. 2017A610104.

Declarations

Conflict of interest The authors declare no competing interests.

References

Atchudan R, Edison T, Aseer KR, Perumal S, Karthik N, Lee YR (2018a) Highly fluorescent nitrogen-doped carbon dots derived from Phyllanthus acidus utilized as a fluorescent probe for label-free selective detection of Fe^{3+} ions, live cell imaging and fluorescent ink. Biosens. Bioelectron. 99:303–311

Atchudan R, Jebakumar Immanuel Edison TN, Perumal S, Lee YR (2018b) Indian gooseberry-derived tunable fluorescent carbon dots as a promise for in vitro/in vivo multicolor bioimaging and fluorescent ink. ACS Omega. 3(12):17590–17601

Chang KE, Kim C, Yoo TJ, Kwon MG, Heo S, Kim SY, Hyun Y, Yoo JI, Ko HC, Lee BH (2019) High responsivity near infrared photodetector using gate modulated graphene/germanium schottky junction. Adv. Electron. Mater. 5(6)

Chen L, Yang G, Wu P, Cai C (2017) Real-time fluorescence assay of alkaline phosphatase in living cells using boron-doped graphene quantum dots as fluorophores. Biosens. Bioelectron. 96:294–299

Chen W, Li D, Tian L, Xiang W, Wang T, Hu W, Hu Y, Chen S, Chen J, Dai Z (2018) Synthesis of graphene quantum dots from natural polymer starch for cell imaging. Green Chem. 20(19):4438–4442

Dutta Chowdhury A, Doong RA (2016) Highly sensitive and selective detection of nanomolar ferric ions using dopamine functionalized graphene quantum dots. ACS Appl. Mater. Interfaces 8(32):21002–210010

Fu Y, Gao G, Zhi J (2019) Electrochemical synthesis of multicolor fluorescent N-doped graphene quantum dots as a ferric ion sensor and their application in bioimaging. Journal of Materials Chemistry B. 7(9):1494–1502

Gao G, Jiang Y-W, Jia H-R, Yang J, Wu F-G (2018) On-off-on fluorescent nanosensor for Fe^{3+} detection and cancer/normal cell differentiation via silicon-doped carbon quantum dots. Carbon 134:232–243

Gong X, Ding X, Jiang N, Zhong T, Wang G (2020) Benzothiazole-based fluorescence chemosensors for rapid recognition and "turn-off" fluorescence detection of Fe^{3+} ions in aqueous solution and in living cells. Microchem. J. 152:104351

Hai X, Guo Z, Lin X, Chen X, Wang J (2018) Fluorescent TPA@GQDs probe for sensitive assay and quantitative imaging of hydroxyl radicals in living cells. ACS Appl. Mater. Interfaces 10(6):5853–5861

Haider G, Roy P, Chiang C-W, Tan W-C, Liou Y-R, Chang H-T, Liang C-T, Shih W-H, Chen Y-F (2016) Electrical-polarization-induced ultrahigh responsivity photodetectors based on graphene and graphene quantum dots. Adv. Funct. Mater. 26(4):620–628

Jia J, Lin B, Gao Y, Jiao Y, Li L, Dong C, Shuang S (2019) Highly luminescent N-doped carbon dots from black soya beans for free radical scavenging, Fe^{3+} sensing and cellular imaging. Spectrochim. Acta A Mol. Biomol. Spectrosc. 211:363–372

Kagit R, Yildirim M, Ozay O, Yesilot S, Ozay H (2014) Phosphazene based multicentered naked-eye fluorescent sensor with high selectivity for Fe^{3+} ions. Inorg. Chem. 53(4):2144–2151

Kaur M, Kaur M, Sharma VK (2018) Nitrogen-doped graphene and graphene quantum dots: a review onsynthesis and applications in energy, sensors and environment. Adv. Colloid Interface Sci. 259:44–64

Khojasteh H, Amiri M, Sohrabi A, Khanahmadzadeh S, Salavati-Niasari M, Moayedi H (2020) Synthesis of magnetically reusable Fe_3O_4/TiO_2-N, P co-doped graphene quantum dot nancomposites using hexachlorocyclophosphazene; high photoluminance property and photocatalytic promoter. J. Mater. Res. Technol. 9(2):1380–1388

Li Y, Shu H, Wang S, Wang J (2015a) Electronic and optical properties of graphene quantum dots: the role of many-body effects. J. Phys. Chem. C 119(9):4983–4989

Li H, Shao F-Q, Zou S-Y, Yang Q-J, Huang H, Feng J-J, Wang A-J (2015b) Microwave-assisted synthesis of N,P-doped carbon dots for fluorescent cell imaging. Microchim. Acta 183(2):821–826

Liu Y, Duan W, Song W, Liu J, Ren C, Wu J, Liu D, Chen H (2017a) Red emission B, N, S-co-doped carbon dots for colorimetric and fluorescent dual mode detection of Fe^{3+} ions in complex biological fluids and living cells. ACS Appl. Mater. Interfaces 9(14):12663–12672

Liu R, Zhao J, Huang Z, Zhang L, Zou M, Shi B, Zhao S (2017b) Nitrogen and phosphorus co-doped graphene quantum dots as a nano-sensor for highly sensitive and selective imaging detection of nitrite in live cell. Sens Actuators B Chem. 240:604–612

Liu Y, Zhao C, Zhao X, Liu H, Wang Y, Du Y, Wei D (2020) A selective N,N-dithenoyl-rhodamine based fluorescent probe for Fe^{3+} detection in aqueous and living cells. J. Environ. Sci. 90:180–188

Lu W, Gong X, Nan M, Liu Y, Shuang S, Dong C (2015) Comparative study for N and S doped carbon dots: Synthesis, characterization and applications for Fe^{3+} probe and cellular imaging. Anal Chim Acta. 898:116–127

Luo Z, Qi G, Chen K, Zou M, Yuwen L, Zhang X, Huang W, Wang L (2016) Microwave-assisted preparation of white fluorescent graphene quantum dots as a novel phosphor for enhanced white-light-emitting diodes. Adv. Funct. Mater. 26(16):2739–2744

Ma Y, Chen AY, Huang YY, He X, Xie XF, He B, Yang JH, Wang XY (2020) Off-on fluorescent switching of boron-doped carbon quantum dots for ultrasensitive sensing of catechol and glutathione. Carbon 162:234–244

Novoselov KS, Geim AK, Morozov SV, Jiang D, Zhang Y, Dubonos SV, Grigorieva IV, Firsov AA (2004) Electric field effect in atomically thin carbon films. Science. 306(5696): 666–669

Pu ZF, Wen QL, Yang YJ, Cui XM, Ling J, Liu P, Cao QE (2020) Fluorescent carbon quantum dots synthesized using phenylalanine and citric acid for selective detection of Fe^{3+} ions. Spectrochim Acta A Mol Biomol Spectrosc. 229:117944

Qu D, Zheng M, Du P, Zhou Y, Zhang L, Li D, Tan H, Zhao Z, Xie Z, Sun Z (2013) Highly luminescent S, N co-doped graphene quantum dots with broad visible absorption bands for visible light photocatalysts. Nanoscale 5(24)

Shi B, Su Y, Zhang L, Huang M, Liu R, Zhao S (2016) Nitrogen and phosphorus co-doped carbon nanodots as a novel fluorescent probe for highly sensitive detection of Fe^{3+} in human serum and living cells. ACS Appl. Mater. Interfaces 8(17): 10717–10725

Sim Y, Kim SJ, Janani G, Chae Y, Surendran S, Kim H, Yoo S, Seok DC, Jung YH, Jeon C, Moon J, Sim U (2020) The synergistic effect of nitrogen and fluorine co-doping in graphene quantum dot catalysts for full water splitting and supercapacitor. Appl. Surf. Sci. 507:145157

Sun X, Bruckner C, Lei Y (2015) One-pot and ultrafast synthesis of nitrogen and phosphorus co-doped carbon dots possessing bright dual wavelength fluorescence emission. Nanoscale 7(41):17278–17282

Wang D, Wang L, Dong X, Shi Z, Jin J (2012) Chemically tailoring graphene oxides into fluorescent nanosheets for Fe^{3+} ion detection. Carbon 50(6):2147–2154

Wang L, Li W, Wu B, Li Z, Wang S, Liu Y, Pan D, Wu M (2016) Facile synthesis of fluorescent graphene quantum dots from coffee grounds for bioimaging and sensing. Chem. Eng. J. 300:75–82

Wang Z, Liu Z, Gu B, Gao B, Wang T, Zheng X, Wang G, Guo Q, Chen D (2020a) Ultraviolet light-driven controllable doping of graphene quantum dots with tunable emission wavelength for fluorescence bio-imaging. Mater. Lett. 266:127468

Wang Z, Chen D, Gu B, Gao B, Liu Z, Yang Y, Guo Q, Zheng X, Wang G (2020b) Yellow emissive nitrogen-doped graphene quantum dots as a label-free fluorescent probe for Fe^{3+} sensing and bioimaging. Diam. Relat. Mater. 104:107749

Xu A, He P, Huang T, Li J, Hu X, Xiang P, Chen D, Yang S, Wang G, Ding G (2018a) Selective supramolecular interaction of ethylenediamine functionalized graphene quantum dots: ultra-sensitive photoluminescence detection for nickel ion in vitro. Synth. Met. 244:106–112

Xu Q, Li B, Ye Y, Cai W, Li W, Yang C, Chen Y, Xu M, Li N, Zheng X, Street J, Luo Y, Cai L (2018b) Synthesis, mechanical investigation, and application of nitrogen and phosphorus co-doped carbon dots with a high photoluminescent quantum yield. Nano Res. 11(7):3691–3701

Yan Y, Liu JH, Li RS, Li YF, Huang CZ, Zhen SJ (2019) Carbon dots synthesized at room temperature for detection of tetracycline hydrochloride. Anal. Chim. Acta 1063:144–151

Yang C-B, Jiang C-B, Zhang M-Y, Chen X, Zou P, Yang R-W, Rao H-B, Wang G-T (2020) A multifunctional Eu-based coordination polymer luminescent sensor for highly sensitive and selective detection of Fe^{3+} and acetone. Polyhedron 175: 114216

Yuan F, Ding L, Li Y, Li X, Fan L, Zhou S, Fang D, Yang S (2015) Multicolor fluorescent graphene quantum dots colorimetrically responsive to all-pH and a wide temperature range. Nanoscale 7(27):11727–11733

Zeng Z, Chen S, Tan TTY, Xiao F-X (2018) Graphene quantum dots (GQDs) and its derivatives for multifarious photocatalysis and photoelectrocatalysis. Catal. Today 315: 171–183

Zhang F, Liu F, Wang C, Xin X, Liu J, Guo S, Zhang J (2016) Effect of lateral size of graphene quantum dots on their properties and application. ACS Appl. Mater. Interfaces 8(3):2104–2110

Zhang M, Su R, Zhong J, Fei L, Cai W, Guan Q, Li W, Li N, Chen Y, Cai L, Xu Q (2019) Red/orange dual-emissive carbon dots for pH sensing and cell imaging. Nano Res. 12(4):815–821

Zhao J, Tang L, Xiang J, Ji R, Yuan J, Zhao J, Yu R, Tai Y, Song L (2014) Chlorine doped graphene quantum dots: preparation, properties, and photovoltaic detectors. Appl. Phys. Lett. 105(11)

Zhu C, Yang S, Wang G, Mo R, He P, Sun J, Di Z, Yuan N, Ding J, Ding G, Xie X (2015) Negative induction effect of graphite N on graphene quantum dots: tunable band gap photoluminescence. J. Mater. Chem. C 3(34):8810–8816